Enhanced Radio-Frequency Sensors Based on a Self-Dual Emitter-Absorber Q2

Minye Yang,[1] Zhilu Ye,[1] Mohamed Farhat,[2] and Pai-Yen Chen[1,*]

[1] *Department of Electrical and Computer Engineering, University of Illinois at Chicago, Chicago, Illinois 60607, United States*

[2] *Computer, Electrical, and Mathematical Science and Engineering Division, King Abdullah University of Science and Technology, Thuwal 23955-6900, Saudi Arabia*

(Received 10 September 2020; revised 18 November 2020; accepted 8 December 2020; published XX XX 2021)

We propose and experimentally demonstrate a parity-time-symmetric electronic system exhibiting the self-dual emitter-absorber property with a remarkable modulation depth in the radio-frequency (rf) region. The dramatically different rf responses between the emitter and absorber modes may allow detection of ultrasmall conductive or reactive perturbations. Our measurement results show that even a perturbation on the order of 10^{-2} can greatly change the system's output intensity by more than 30 dB, consistent with the theoretical prediction. The measured sensitivity is far beyond the sensitivity of traditional sensors based on a Fabry-Perot resonator, and may lead to monotonic rf sensors with high sensitivity and resolvability.

DOI: 10.1103/PhysRevApplied.0.XXXXXX

I. INTRODUCTION

In the past decade, non-Hermitian physics, exemplified by parity-time (PT) symmetry, has gained tremendous attention in the fields of quantum mechanics [1], optics, photonics [2–9], acoustics [10,11], and electronics [12–17]. These physical systems share a common feature: that is, non-Hermitian degeneracy and exceptional points (EPs) where the Taylor-series expansion fails to converge in the multivalued complex eigenspectrum. The appearance of branching singularities at EPs [7–9,18] has led to a variety of sensing [17–25], imaging [26,27], information-processing [28–34], and wireless-power-transfer [35,36] applications. Besides, another unusual kind of singularity, a coherent-perfect-absorber–laser (CPAL) point, can be observed in PT-symmetric systems [6,37–42] constituted by coupled gain and loss oscillators. Traditionally, a laser oscillator emits coherent outgoing radiation, while a CPA is a dark medium absorbing all incoming radiation (i.e., the time-reversed counterpart of a laser). However, at the CPAL point of PT-symmetric systems, the laser and CPA modes, which exhibit completely different scattering properties, can be switched at will through adjustment of the initial phase difference of two counterpropagating monotonic input waves. Experimental observations of such a self-dual singularity have been reported in optics and photonics [6,38], which show great promise for building next-generation optical switches and interferometers [6,37–42].

Sensing may be one of the most-interesting applications of non-Hermitian devices with exotic spectral singularities. Several groups have demonstrated that singular points in PT-symmetric systems, such as EPs that cause the eigenvalue-bifurcation effect, can be exploited to boost the resonance frequency shift and thus sensitivity of rf or optical sensors [17–24]. However, it has been reported that EP-based sensors could be rather vulnerable to phase noise and flicker noise, as well as modal interference occurring near a higher-order EP [43–45], and could result in low spectrum or bandwidth efficiency, especially in the radio-wave region. Very recently, we theoretically proposed a monotonic (or monochromatic) optical sensor operating at the CPAL point for mitigating the noise and spectral efficiency issues observed in EP-based sensors [43–46]. Differently from EP-based sensors, which monitor the shift of resonant peaks due to the eigenvalue bifurcation, the CPAL-based sensor adopts a monotonic sensing scheme and detects the output intensity as a function of the impedance perturbation at a given frequency [46]. In this Letter, we further provide an experimental demonstration of CPAL-based PT-symmetric sensors with enhanced sensitivity in the radio-frequency (rf) range.

Figures 1(a) and 1(b) present the schematics and a circuit diagram of the proposed PT-symmetric rf sensor, which consists of a lossy component with conductance G Q3 and an amplifying component with an effective negative conductance $-G$ [e.g., a negative-impedance converter (NIC)]. These gain and loss elements are separated by an electrical length $x = \pi/2 + \delta x$, which can be realized with a transmission-line segment or a compact T/Π equivalent Q4 circuit [Fig. 1(b)]. To achieve the CPAL effect, the conductances must be tuned to $G = |-G| = \sqrt{2}Y_0$, where Q5 Y_0 is the characteristic admittance of the transmission-line segment [46]. The scattering matrix $\mathbf{S}$ can be used

*pychen@uic.edu

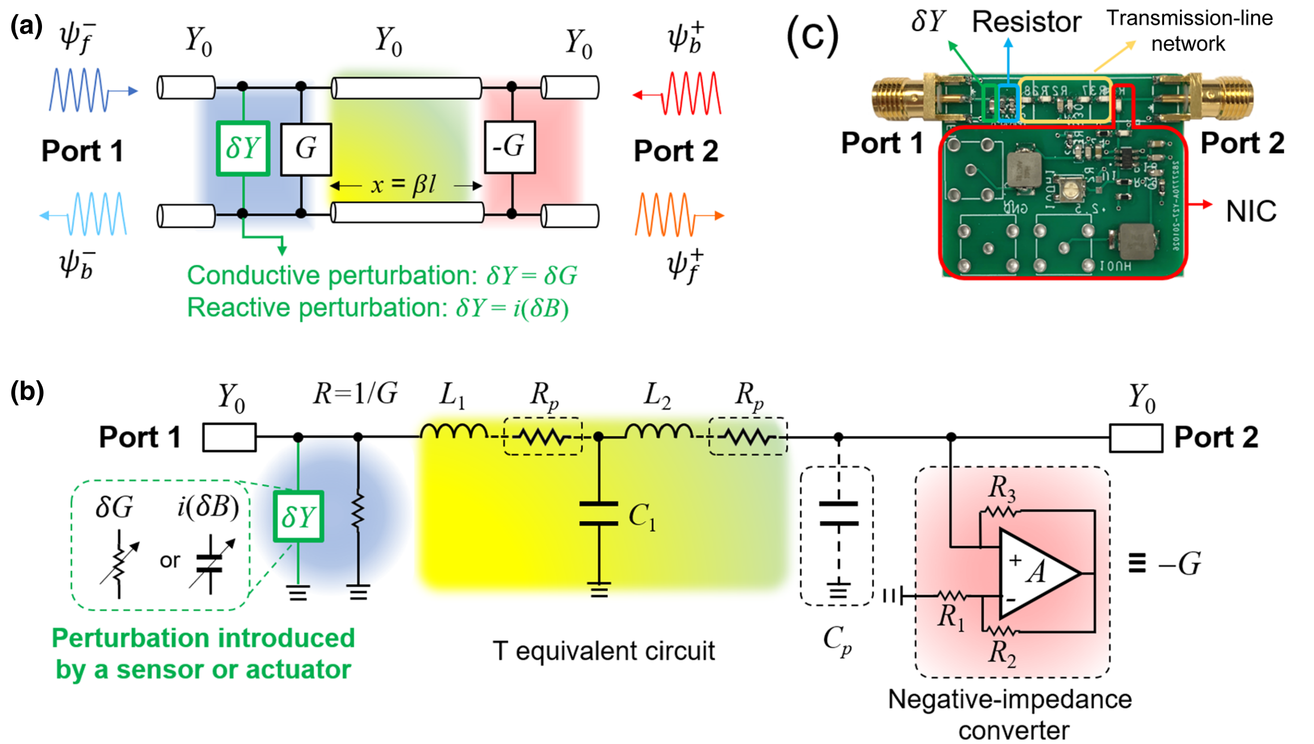

FIG. 1. (a) Equivalent-transmission-line model for the generalized *PT*-symmetric system and (b) its practical realization in the rf range; here a shunt resistor or capacitor of different values (i.e., pseudosensor) is used to mimic the impedance variations in a sensing or actuation element. (c) Photograph of the CPAL-locked *PT*-symmetric rf circuit in (b), realized with the PCB technique.

to connect the input and output voltage signals in the left (−) and right (+) ports: $|\psi_{\text{out}}\rangle = \mathbf{S}|\psi_{\text{in}}\rangle$, where $|\psi_{\text{in}}\rangle = (\psi_f^-, \psi_b^+)^T$ and $|\psi_{\text{out}}\rangle = (\psi_b^-, \psi_f^+)^{\text{T}}$ [Fig. 1(a)]. At the CPAL frequency (ω_0), the two eigenvalues of $\mathbf{S}$ ($\lambda_\pm$) will diverge into zero (i.e., CPA mode) and infinity (i.e., laser mode); see Appendix A. Such a self-dual spectral singularity can be seen in Fig. 2(a), where $\delta x = 10^{-2}\pi/2$. When a small impedance perturbation δY is introduced, this electronic *PT* system can be switched from CPA mode to laser mode and vice versa, resulting in a dramatic change in the output intensity. This property can be exploited to build types of rf and microwave sensors with ultrahigh sensitivity. The laser and CPA modes can be characterized by the output coefficient Θ, defined as the ratio of the total output power to the total input power:

$$\Theta = \frac{|\psi_b^-|^2 + |\psi_f^+|^2}{|\psi_f^-|^2 + |\psi_b^+|^2}. \tag{1}$$

When the voltage ratio of two input waves $\psi_b^+/\psi_f^- = i(\sqrt{2}-1)$, the CPA mode ($\Theta \approx 0$) can be achieved, while the emitter mode is obtained at any other ψ_b^+/ψ_f^- value. Let us first consider the conductive (resistive) sensing scenario, where the electronic circuit in Fig. 1(b) initially works in the CPA mode and a small conductive perturbation δG is introduced to the loss side. The output coefficient as a function of the conductive perturbation and the intentional phase offset δx can be expressed as

$$\Theta_{PT} \approx \frac{1}{4}\left((\delta x)^2 + \frac{\nu^2}{(\delta x)^2}\right) + O(\nu^3), \tag{2}$$

where $\nu = \delta G/Y_0 \ll 1$ (see Appendix B for detailed derivations of the output coefficients). From Eq. (2), it is clear that in the small-perturbation regime, the sensitivity may be boosted by an augmentation factor, $1/(\delta x)^2$. As ν increases, the output coefficient will rapidly converge to max $\Theta_{PT} = 3 + 2\sqrt{2}$. Here we also examine the sensor based on a Fabry-Perot (FP) resonator formed by a pair of lumped elements with conductances $G = \sqrt{2}Y_0$ separated from each other by electrical length $x = \pi + \delta x$. When $\psi_b^+/\psi_f^- = -1$, the FP resonator behaves like a CPA. Under small conductive perturbation, the output coefficient of the FP-type sensor is given by

$$\Theta_{\text{Fabry - Perot}} \approx \left(3 - 2\sqrt{2}\right)^2 (1 + 2\nu^2) + O(\nu^3). \tag{3}$$

Comparing Eqs. (2) and (3), we find that sensors based on the CPAL-locked electronic *PT* dimer can outperform the sensor based on the conventional FP resonator in terms of sensitivity and modulation depth because of the augmentation factor $1/(\delta x)^2$, which sharpens the

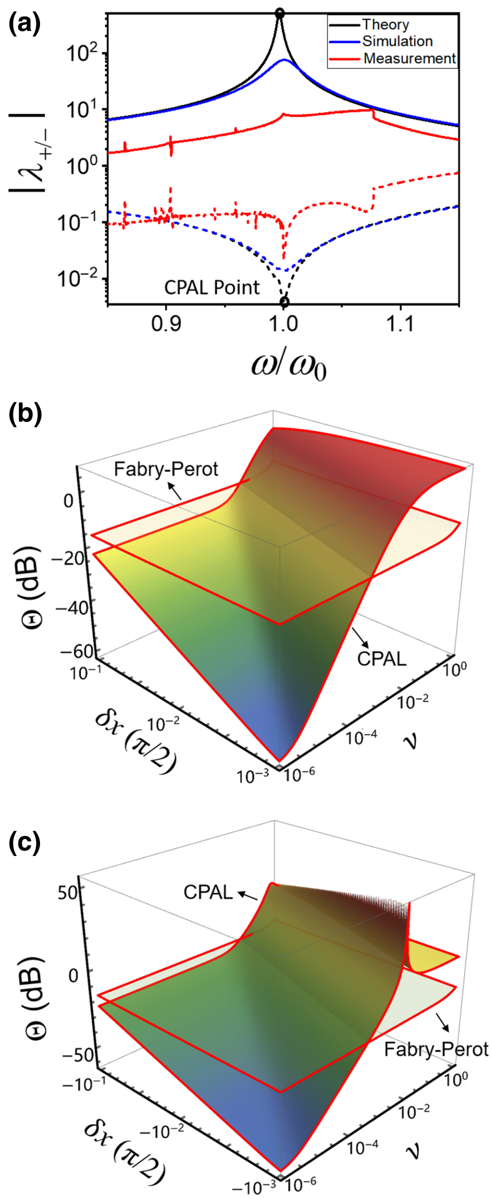

FIG. 2. (a) Evolution of the eigenvalues as a function of the normalized frequency for the PT-symmetric electronic circuit in Fig. 1; here $G = |-G| = \sqrt{2}Y_0$ and $x(\omega_0) = 0.99\pi/2$. The measurement (red lines) and simulation (blue lines) results are in a good agreement at the CPAL point. Contours of the output coefficient as a function of conductive perturbation ν for the CPAL-locked PT-symmetric system in Fig. 1(a) and a passive Fabry-Perot resonator, with (b) positive phase offset δx and (c) negative phase offset$-\delta x$.

derivative of $\Theta_{PT}(\nu)$. Such an effect can be clearly observed in Figs. 2(b) and 2(c), which present contours of Θ as a function of ν and δx for the CPAL-locked sensor and the FP-type sensor.

In the same vein, under small reactive perturbation ($i\delta B$), the output coefficient of the CPAL-locked sensor and the FP-type sensor can be expressed as

$$\Theta_{PT} \approx \frac{1}{4}\left((\delta x)^2 + \frac{\mu^2}{(\delta x)^2}\right) + O(\mu^3), \tag{4}$$

$$\Theta_{\text{Fabry - Perot}} \approx \left(3 - 2\sqrt{2}\right)^2 + (17\sqrt{2} - 24)\mu^2 + O(\mu^3), \tag{5}$$

where $\mu = \delta B/Y_0 \ll 1$. Again, it is evident from Eq. 4(a) that the sensitivity related to the first derivative of $\Theta_{PT}(\mu)$ can be enhanced by a factor of $1/(\delta x)^2$. Such an enhancement of sensitivity is, however, not obtained in FP-type sensors.

In this work, we build a laboratory prototype of the CPAL-locked electronic circuit on a printed circuit board (PCB). The schematics and a photograph of the PCB are shown in Figs. 1(b) and 1(c). In our design, positive and negative shunt conductances are realized with a resistor and a NIC based on the feedback structure and a high-speed operational amplifier (OPA355). At 13.48 MHz, the Q6 effective impedances of the NIC and the resistor are measured to be $-35.56 - 0.18i\ \Omega$ and $35.4\ \Omega$, respectively; here we use the $e^{i\omega t}$ notation. The equivalent impedance and electrical length of the T-equivalent network are Y_0 and $x = \pi/2 + \delta x$, where $\delta x \sim 3\pi/40$. The PCB is connected to a two-port vector network analyzer with input conductance $Y_0 = 1/50$ S. This setup allows the system to operate near the CPAL point obtained when $G = |-G| = \sqrt{2}Y_0$ and $x = \pi/2$. To generate the conductive (reactive) perturbation to mimic a sensor or actuator with variable effective resistance (capacitance) [13,17–20], a shunt resistor (capacitor) of admittance δG ($i\delta B$) is added to the onboard PT-symmetric circuit; see Appendix C for the detailed implementation and measurement. Figure 2(a) compares the measured and simulated eigenvalues of the CPAL-locked circuit, showing good agreement between both results near the CPAL point. In our simulation, the circuit simulation is performed with ADVANCED DESIGN SYSTEM, with a realistic operational-amplifier mode [47, 48]. In addition, the parasitic capacitance C_p and the parasitic resistance R_p existing in inductors L_1 and L_2 and the NIC are added in the PT circuit, as can be seen in Fig. 1(b).

Figures 3(a) and 3(b) present the measured S parameters for the PT circuit in Fig. 1(c) under conductive and reactive perturbation, respectively; here the effect of C_p and R_p is already taken into consideration. It can be seen from Fig. 3 that the measurement (points) and simulation results (dashed lines) are in good agreement. Without loss of generality, the output coefficients can be obtained from the measured S parameters (see Appendix C for details). For comparison, the rf FP resonator sketched in the inset in Fig. 4 is fabricated and measured. The electronic FP resonator is formed by a pair of resistors

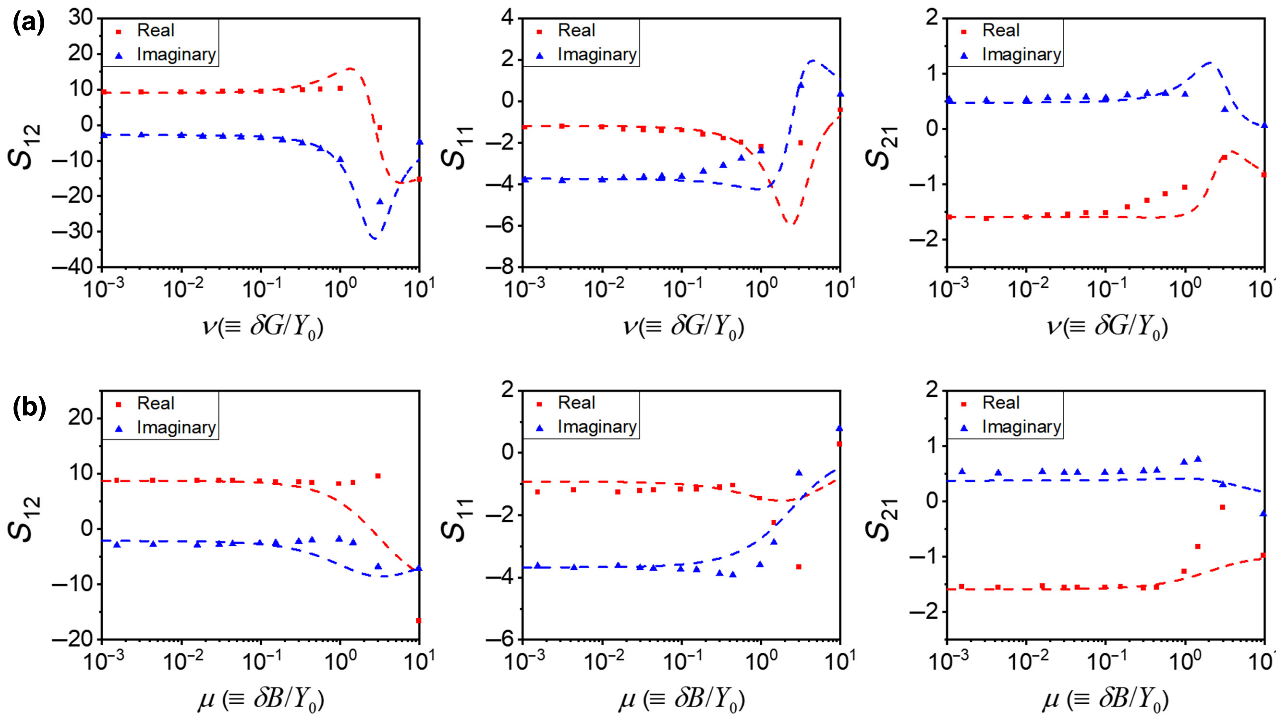

FIG. 3. Measured (points) and simulated (dashed lines) real (red) and imaginary (blue) parts of the S parameters under (a) conductive and (b) reactive perturbation. For both cases, the simulation results agree well with the measured ones in the working range. The simulation is based on the equivalent-circuit model in Fig. 1(b), with the effective parasitic capacitance and a realistic SPICE model for the operational amplifier.

with $R = 35.4\ \Omega$ and a T-equivalent network with $x \approx \pi$. Figures 4(a) and 4(b), respectively, depict the output coefficients Θ_{PT} and $\Theta_{\text{Fabry - Perot}}$ under conductive and reactive perturbations (i.e., by our loading the circuit with different shunt resistors and capacitors); for each data point, the measurement is repeated by eight times to plot the root-mean-square error. The measurement and simulation results are in good agreement, showing that

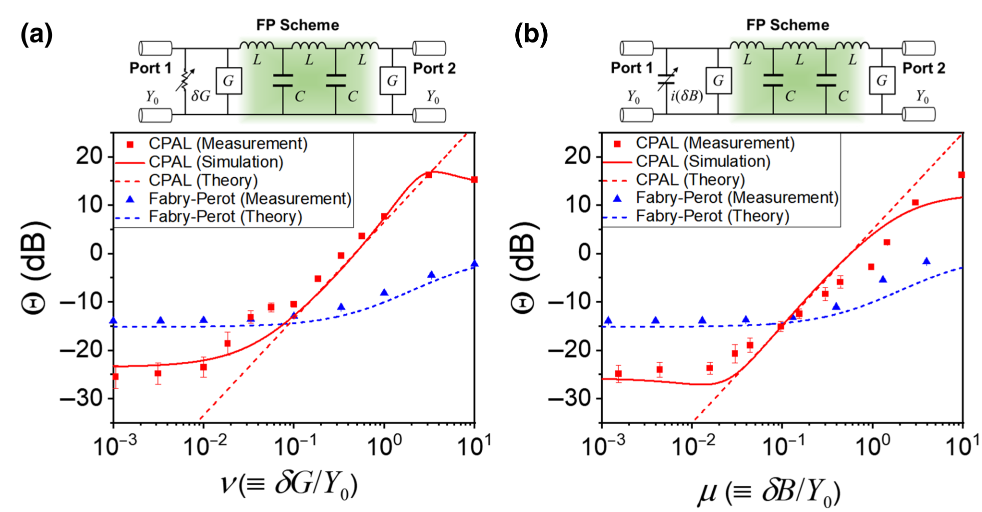

FIG. 4. (a) Output coefficient versus conductive perturbation $\nu = \delta G/Y_0$ for the CPAL-locked (red lines) and FP (blue lines) rf sensors sketched in the inset; here the points, solid lines, and dashed lines represent the measurement, simulation, and theoretical results [according to Eqs. (2) and (3)], respectively. When plotting the theoretical predictions, we used the phase offset $\delta x = 3\pi/40$ to fit the measurement results. The maximal error bar of the CPAL sensor is below 2.4 dB. (c) Similar to (b) but for reactive perturbation $\mu = i(\delta B)/Y_0$; here the theoretical prediction is based on Eq. (4).

the slope of the output-coefficient curve of the CPAL-locked circuit is remarkably larger than that of the FP-type circuit. As a result, the CPAL-locked rf sensor may be capable of detecting small conductive and reactive perturbations, well beyond the limitation of current passive rf sensors. We note that there are slight discrepancies between the measured and simulated output coefficients, which could be attributed to fabrication errors and the parasitics of lumped elements mounted on the PCB, such as C_p, R_p, board defects, and SMA-connector flaws. In practice, the above-mentioned issues can be mitigated by use of complementary-metal-oxide-semiconductor (CMOS) and integrated-circuit technologies. For on-chip NIC modules (e.g., a cross-coupled pair, which is commonly used in analog and rf integrated-circuits) and sensors, parasitic elements could be partially or fully removed, and therefore the root-mean-square error can be further minimized. Besides, through the on-chip techniques, the intentional phase offset (δx) of an equivalent network can be precisely controlled. As a result, on-chip techniques may allow one to push the sensitivity and detection limits of the CPAL-locked PT-symmetric sensor. To practically implement the proposed sensor initially locked in the CPA state, a high-resolution tunable phase shifter, such as those made of CMOS or microelectromechanical-system (MEMS) technologies, and an attenuator are required at a terminal of this rf circuit. The proposed CPAL sensor may be beneficial for various sensing scenarios. For example, in rf biosensing applications [49], a trapped living cell generally changes the reflection or transmission coefficient of a transmission-line segment by less than 0.5 dB. However, the same cell, if regarded as a chemiresistance perturbation, could lead to a change in the output coefficient of the CPAL sensor on the order of tens of decibels, which implies much-increased sensitivity, detectability, and noise immunity.

Finally, we note that the proposed CPAL-locked PT-symmetric sensor with the equivalent-transmission-line model sketched in Fig. 1(a) can also be implemented in the optical domain, where the gain and loss elements could be realized with active and passive metasurfaces [24,38] and the phase offset is determined by the thickness of the dielectric spacer or air gap.

To sum up, we experimentally demonstrate a CPAL-locked PT-symmetric electronic circuitry that can be used to build monotonic rf sensors capable of detecting subtle impedance changes with high sensitivity. At the CPAL point, a small conductive or reactive disturbance in the sensing or actuation element can result in substantial changes in the output intensity. Our measurement results show that the proposed sensor can detect conductive and capacitive perturbations on the order of 10^{-2}, which is not possible with a passive rf sensor based on a classical Fabry-Perot resonator. With further development and optimization of the electronic PT system using CMOS and/or on-chip MEMS technologies, the CPAL-based sensing mechanism could be used to build next-generation ultrasensitive rf and microwave sensors and could be readily extended to interferometric optical sensors based on monotonic lights.

ACKNOWLEDGMENTS

P.-Y.C. thanks the U.S. NSF (Grant No. ECCS-1711409) for supporting this work.

APPENDIX A: SCATTERING PROPERTIES AND THE CPAL CONDITION OF THE *PT* CIRCUIT

The scattering matrix $\mathbf{S}$ of the PT-symmetric two-port transmission-line network in Fig. 1(a), with $G=\sqrt{2}Y_0$ and $-G=-\sqrt{2}Y_0$, can be derived as

$$\mathbf{S}=\begin{pmatrix} \sec x & i\left(1+\sqrt{2}\right)\tan x \\ i\left(1-\sqrt{2}\right)\tan x & \sec x \end{pmatrix}. \tag{A1}$$

The CPAL point occurs when $x=\pi/2$. Throughout this study, we use the $e^{i\omega t}$ notation. The eigenvalues of $\mathbf{S}$ can be written as

$$\lambda_{\pm}=\sec\left(\frac{\pi\omega}{2\omega_0}\right)\pm\tan\left(\frac{\pi\omega}{2\omega_0}\right), \tag{A2}$$

where ω is the angular frequency and ω_0 is the angular design frequency (frequency at CPAL point).

APPENDIX B: RESPONSE OF THE OUTPUT COEFFICIENT TO IMPEDANCE PERTURBATIONS

When a conductive perturbation $\nu=\delta G/Y_0$ is applied to the PT circuit in Fig. 1(b) initially operating in CPA mode [i.e., $\psi_{\mathrm{b}}^{+}/\psi_{\mathrm{f}}^{-}=\mathrm{i}(\sqrt{2}-1)$], the output coefficient in response to ν can be derived as

$$\begin{aligned}\Theta_{PT}&=\frac{2\sqrt{2}\nu(\sec\delta x-1)-4(\sec\delta x-1)^2-\nu^2\sec^2\delta x}{(2\sqrt{2}-3)\nu^2-(\nu+2)^2\tan^2\delta x}\\ &\approx\frac{1}{4}\left((\delta x)^2+\frac{\nu^2}{(\delta x)^2}-\frac{(8-3\sqrt{2})}{4}\frac{\nu^3}{(\delta x)^2}+O(\nu^4)\right)\\ &\quad \mathit{if}\quad \nu\ll 1\\ &\approx\frac{1}{4}\left((\delta x)^2+\frac{\nu^2}{(\delta x)^2}\right)+O(\nu^3).\end{aligned} \tag{B1}$$

Similarly, the output coefficient as a function of ν for a Fabry-Perot CPA with $\psi_b^{+}/\psi_f^{-}=-1$ can be derived as

$$\Theta_{\text{Fabry - Perot}} = \frac{\csc\delta x \begin{pmatrix} 4i\left(2+\sqrt{2}\nu\right) - 2i[4\sqrt{2}+\nu(6+\sqrt{2}\nu)]\cos\delta x \\ +4\left(2\sqrt{2}+\nu\right)\cot\delta \mathrm{x} \\ +\left[-6+\nu^2-2\left(3+2\sqrt{2}\nu+\nu^2\right)\cos\delta x\right]\csc\delta x \end{pmatrix}}{\left[4+2\sqrt{2}+\nu+\sqrt{2}\nu-i\left(2+2\sqrt{2}+\nu\right)\cot\delta x\right]^2}$$
$$\approx \left(\frac{2(\sqrt{2}-1)+\nu}{2(\sqrt{2}+1)+\nu}\right)^2 \quad \mathit{if} \quad \nu \ll 1$$
$$\approx \left(3-2\sqrt{2}\right)^2(1+2\nu^2)+O(\nu^3). \tag{B2}$$

When the reactive perturbation ($\mu = \delta B/Y_0$) is considered, the output coefficients of the CPAL-locked PT circuit (initially set to the CPA mode) and the Fabry-Perot CPA are given by

$$\Theta_{PT} = \frac{4-\sec\delta x[8-(\mu^2+4)\sec\delta x]}{(2\sqrt{2}-3)\mu^2-4(\sqrt{2}-1)\mu\tan\delta x+(\mu^2+4)\tan^2\delta x}$$
$$\approx \frac{1}{4}\left((\delta x)^2+\frac{\mu^2}{(\delta x)^2}\right)+O(\mu^3) \quad \mathit{if} \quad \mu \ll 1 \tag{B3}$$

and

$$\Theta_{\text{Fabry - Perot}} = \frac{\left[\begin{pmatrix} 2\left(5+2\sqrt{2}\mu+\mu^2\right)-4\left(2\sqrt{2}+\mu\right)\cos\delta x \\ -(-2+\mu^2)\cos 2\delta x \end{pmatrix}\csc{(\delta x)}^2\right]}{\begin{pmatrix} 4\left(3+2\sqrt{2}\right)[2+\cot{(\delta x)}^2]+\mu^2\left[3+2\sqrt{2}+\cot{(\delta x)}^2\right] \\ +4\mu\left[4+3\sqrt{2}+\left(1+\sqrt{2}\right)\cot^2(\delta x)\right] \end{pmatrix}}$$
$$\approx \left(\frac{\sqrt{2}-1}{\sqrt{2}+1}\right)^2+\frac{\sqrt{2}\mu^2}{(\sqrt{2}+1)^4}+\frac{2\sqrt{2}\mu}{(\sqrt{2}+1)^4}\delta \mathrm{x}+O(\mu^3) \quad \mathit{if} \quad \mu \ll 1$$
$$\approx \left(3-2\sqrt{2}\right)^2+(17\sqrt{2}-24)\mu^2+O(\mu^3). \tag{B4}$$

The CPA-like phenomena can be observed in a passive FP resonator when $\psi_b^+/\psi_f^- = -1$, for which the eigenvalues are zero and unitary at the CPA point.

APPENDIX C: IMPLEMENTATION AND MEASUREMENT OF THE ONBOARD CPAL-LOCKED RF SENSOR

In electronics, negative resistance can be obtained from the active NIC sketched schematically in Fig. 1(b), whose effective negative resistance is given by

$$-R = -R_3\frac{R_1}{R_2}, \tag{C1}$$

where R_1, R_2, and R_3 are labeled in Fig. 1(b) and an ideal operational amplifier with infinite open-loop gain is assumed. In our design, R_1 and R_2 are chosen to be 500 Ω, R_3 is given by an adjustable trimmer potentiometer with maximum resistance of 100 Ω, and a commercial operational amplifier (OPA355) is used to form a feedback loop, as shown in Fig. 1(b). Figure 5(a) plots the measured effective (shunt) impedance of this NIC. At the operating frequency (ω_0 = 13.48 MHz), the effective impedance is $-35.56-0.18i$ Ω, which is quite close to the target value of $-25\sqrt{2}\Omega$. For minimize the device area, a transmission-line segment with characteristic impedance of 50 Ω and electrical length of x at the design frequency ω_0 can be replaced by the T-equivalent network formed by two series inductors and a shunt capacitor [see Fig. 1(b)], which are

$$C_1 = \frac{Y_0}{\omega_0\sin x} \text{ and } L_1 = L_2 = \frac{\sin x}{Y_0\omega_0(1-\cos x)}. \tag{C2}$$

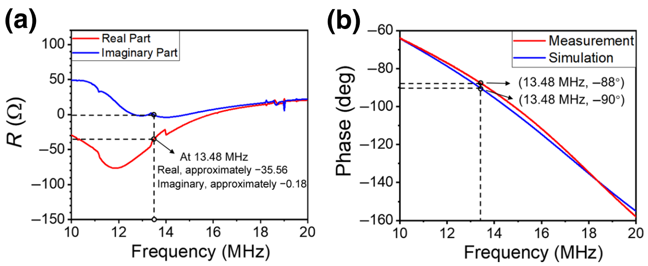

FIG. 5. (a) Real (red line) and imaginary (blue line) parts of the measured impedance of the NIC. At 13.48 MHz, the input impedance is $-35.56 - 0.18i\ \Omega$, which is close to the value required for the CPAL condition ($-25\sqrt{2}\ \Omega$.). (b) Measured (red line) and simulated (blue line) electrical length of the T-equivalent network. At the design frequency of 13.48 MHz, the measured electrical length is $-88°$.

To observe the CPAL effect at 13.48 MHz, $C_1 = 236.1$ pF ≈ 236 pF and $L_1 = L_2 = 590.3$ nH ≈ 590 nH are chosen; here 220- and 16-pF capacitors are connected in parallel to achieve the desired capacitance, while 470- and 120-nH inductors are connected in series to achieve the required inductance. Besides, the inductors have a total intrinsic resistance of 5 Ω (R_p). Figure 5(b) presents the measured and simulated electrical length of this T-equivalent network, showing an electrical length $x = -88^o$ at the operating frequency and a phase offset $\delta x = -2^o$ *or* $-\pi/90$. Fabrication tolerance of lumped elements and interconnection lines as well as parasitics in the NIC and SMA connectors contributed partially to the phase offset. Thus, when the equivalent network is integrated with the gain and loss elements, the phase offset is extracted to be $\delta x\ \sim 3\pi/40$. To mimic the resistive perturbation in a sensing or actuation element, a shunt resistor ($R = 1/\delta G$) or a shunt capacitor ($C = \delta G/\omega_0$) is added to the *PT*-symmetric pseudosensing circuit. The output coefficient of the two-port *PT*-symmetric circuit can be expressed as

$$\Theta = \frac{|\psi_b^-|^2 + |\psi_f^+|^2}{|\psi_f^-|^2 + |\psi_b^+|^2} = \frac{|1 + \alpha(S_{12}/S_{11})|^2 + |\alpha + S_{21}/S_{11}|^2}{(1 + |\alpha|^2)\ |1/S_{11}|^2}, \tag{C3}$$

where $\alpha = \psi_b^+/\psi_f^-$ and S parameters can be found in Appendix A. Without loss of generality, the output coefficients reported in Figs. 4(a) and 4(b) are obtained by our substituting the measured S parameters (Fig. 3) into Eq. (C3) and assuming $\alpha = i(\sqrt{2} - 1)$. The **S** matrix is characterized by our using a two-port vector network analyzer.

[1] C. M. Bender and S. Boettcher, Real Spectra in Non-Hermitian Hamiltonians Having PT Symmetry, Phys. Rev. Lett. **80**, 5243 (1998).
[2] R. El-Ganainy, K. G. Makris, M. Khajavikhan, Z. H. Musslimani, S. Rotter, and D. N. Christodoulides, Non-Hermitian physics and PT symmetry, Nature Phys. **14**, 11 (2018).
[3] C. E. Rüter, K. G. Makris, R. El-Ganainy, D. N. Christodoulides, M. Segev, and D. Kip, Observation of parity–time symmetry in optics, Nature Phys. **6**, 192 (2010).
[4] H. Ramezani, T. Kottos, R. El-Ganainy, and D. N. Christodoulides, Unidirectional nonlinear PT-symmetric optical structures, Phys. Rev. A **82**, 043803 (2010).
[5] R. El-Ganainy, K. G. Makris, D. N. Christodoulides, and Z. H. Musslimani, Theory of coupled optical PT-symmetric structures, Opt. Lett. **32**, 2632 (2007).
[6] Y. D. Chong, L. Ge, and A. D. Stone, PT-Symmetry Breaking and Laser-Absorber Modes in Optical Scattering Systems, Phys. Rev. Lett. **106**, 093902 (2011).
[7] Ş. K. Özdemir, S. Rotter, F. Nori, and L. Yang, Parity-Time symmetry and exceptional points in photonics, Nat. Mater. **18**, 783 (2019).
[8] M.-A. Miri and A. Alù, Exceptional points in optics and photonics, Science **363**, eaar7709 (2019).
[9] A. Guo, G. J. Salamo, D. Duchesne, R. Morandotti, M. Volatier-Ravat, V. Aimez, G. A. Siviloglou, and D. N. Christodoulides, Observation of PT-Symmetry Breaking in Complex Optical Potentials, Phys. Rev. Lett. **103**, 093902 (2009).
[10] R. Fleury, D. Sounas, and A. Alù, An invisible acoustic sensor based on parity-time symmetry, Nat. Commun. **6**, 5905 (2015).
[11] X. Zhu, H. Ramezani, C. Shi, J. Zhu, and X. Zhang, PT-Symmetric Acoustics, Phys. Rev. X. **4**, 031042 (2014).
[12] J. Schindler, Z. Lin, J. M. Lee, H. Ramezani, F. M. Ellis, and T. Kottos, PT-Symmetric Electronics, J. Phys. A: Math. Theor. **45**, 444029 (2012).
[13] J. Schindler, A. Li, M. C. Zheng, F. M. Ellis, and T. Kottos, Experimental study of active LRC circuits with PT symmetries, Phys. Rev. A **84**, 040101 (2011).
[14] Y. Ra'di, D. L. Sounas, A. Alù, and S. A. Tretyakov, Parity-time-symmetric teleportation, Phys. Rev. B **93**, 235427 (2016).
[15] J. M. Lee, S. Factor, Z. Lin, I. Vitebskiy, F. M. Ellis, and T. Kottos, Reconfigurable Directional Lasing Modes in Cavities with Generalized PT Symmetry, Phys. Rev. Lett. **112**, 253902 (2014).
[16] Z. Ye, M. Farhat, and P.-Y. Chen, Tunability and switching of fano and lorentz resonances in PTX-symmetric electronic systems, Appl. Phys. Lett. **117**, 031101 (2020).
[17] P.-Y. Chen, M. Sakhdari, M. Hajizadegan, Q. Cui, M. M.-C. Cheng, R. El-Ganainy, and A. Alù, Generalized parity–time symmetry condition for enhanced sensor telemetry, Nat. Electron **1**, 297 (2018).
[18] M. Sakhdari, M. Hajizadegan, Q. Zhong, D. N. Christodoulides, R. El-Ganainy, and P.-Y. Chen, Experimental Observation of PT Symmetry Breaking Near Divergent Exceptional Points, Phys. Rev. Lett. **123**, 193901 (2019).
[19] Z. Dong, Z. Li, F. Yang, C.-W. Qiu, and J. S. Ho, Sensitive readout of implantable microsensors using a wireless

system locked to an exceptional point, Nat. Electron **2**, 335 (2019).

[20] M. Sakhdari, M. Hajizadegan, Y. Li, M. M.-C. Cheng, J. C. H. Hung, and P.-Y. Chen, Ultrasensitive, parity–time-symmetric wireless reactive and resistive sensors, IEEE Sensors J. **18**, 9548 (2018).

[21] M. C. Rechtsman, Optical sensing gets exceptional, Nature **548**, 161 (2017).

[22] W. Chen, Ş Kaya Özdemir, G. Zhao, J. Wiersig, and L. Yang, Exceptional points enhance sensing in an optical microcavity, Nature **548**, 192 (2017).

[23] P.-Y. Chen and R. El-Ganainy, Exceptional points enhance wireless readout, Nat. Electron **2**, 323 (2019).

[24] P.-Y. Chen and J. Jung, PT symmetry and Singularity-Enhanced Sensing Based on Photoexcited Graphene Metasurfaces, Phys. Rev. Appl. **5**, 064018 (2016).

[25] M. Hajizadegan, M. Sakhdari, S. Liao, and P.-Y. Chen, High-Sensitivity wireless displacement sensing enabled by PT-symmetric telemetry, IEEE Transactions on Antennas and Propagation **67**, 3445 (2019).

[26] R. Fleury, D. L. Sounas, and A. Alù, Negative Refraction and Planar Focusing Based on Parity-Time Symmetric Metasurfaces, Phys. Rev. Lett. **113**, 023903 (2014).

[27] X. Lin, Y. Yang, N. Rivera, J. J. López, Y. Shen, I. Kaminer, H. Chen, B. Zhang, J. D. Joannopoulos, and M. Soljačić, All-Angle negative refraction of highly squeezed plasmon and phonon polaritons in graphene–boron nitride heterostructures, Proc. Natl. Acad. Sci. USA, 201701830 (2017).

[28] Z. Lin, H. Ramezani, T. Eichelkraut, T. Kottos, H. Cao, and D. N. Christodoulides, Unidirectional Invisibility Induced by PT-Symmetric Periodic Structures, Phys. Rev. Lett. **106**, 213901 (2011).

[29] L. Chang, X. Jiang, S. Hua, C. Yang, J. Wen, L. Jiang, G. Li, G. Wang, and M. Xiao, Parity–time symmetry and variable optical isolation in active–passive-coupled microresonators, Nat. Photon **8**, 524 (2014).

[30] L. Feng, Y.-L. Xu, W. S. Fegadolli, M.-H. Lu, J. E. B. Oliveira, V. R. Almeida, Y.-F. Chen, and A. Scherer, Experimental demonstration of a unidirectional reflectionless parity-time metamaterial at optical frequencies, Nature Mater **12**, 108 (2013).

[31] S. Savoia, G. Castaldi, V. Galdi, A. Alù, and N. Engheta, Tunneling of obliquely incident waves through PT-symmetric epsilon-near-zero bilayers, Phys. Rev. B **89**, 085105 (2014).

[32] J. Doppler, A. A. Mailybaev, J. Böhm, U. Kuhl, A. Girschik, F. Libisch, T. J. Milburn, P. Rabl, N. Moiseyev, and S. Rotter, Dynamically encircling an exceptional point for asymmetric mode switching, Nature **537**, 76 (2016).

[33] S. Savoia, G. Castaldi, and V. Galdi, Non-Hermiticity-Induced wave confinement and guiding in loss-gain-loss three-layer systems, Phys. Rev. A **94**, 043838 (2016).

[34] D. L. Sounas, R. Fleury, and A. Alù, Unidirectional Cloaking Based on Metasurfaces with Balanced Loss and Gain, Phys. Rev. Appl. **4**, 014005 (2015).

[35] S. Assawaworrarit, X. Yu, and S. Fan, Robust wireless power transfer using a nonlinear parity–time-symmetric circuit, Nature **546**, 387 (2017).

[36] M. Sakhdari, M. Hajizadegan, and P.-Y. Chen, Robust extended-range wireless power transfer using a higher-order PT-symmetric platform, Phys. Rev. Res. **2**, 013152 (2020).

[37] S. Longhi, PT -Symmetric laser absorber, Phys. Rev. A **82**, 031801 (2010).

[38] M. Sakhdari, N. M. Estakhri, H. Bagci, and P.-Y. Chen, Low-Threshold Lasing and Coherent Perfect Absorption in Generalized P T -Symmetric Optical Structures, Phys. Rev. Appl. **10**, 024030 (2018).

[39] Z. J. Wong, Y.-L. Xu, J. Kim, K. O'Brien, Y. Wang, L. Feng, and X. Zhang, Lasing and anti-lasing in a single cavity, Nature Photon **10**, 796 (2016).

[40] L. Feng, Z. J. Wong, R.-M. Ma, Y. Wang, and X. Zhang, Single-Mode laser by parity-time symmetry breaking, Science **346**, 972 (2014).

[41] H. Hodaei, M.-A. Miri, M. Heinrich, D. N. Christodoulides, and M. Khajavikhan, Parity-Time-Symmetric microring lasers, Science **346**, 975 (2014).

[42] Y. Sun, W. Tan, H. Li, J. Li, and H. Chen, Experimental Demonstration of a Coherent Perfect Absorber with PT Phase Transition, Phys. Rev. Lett. **112**, 143903 (2014).

[43] Z. Xiao, H. Li, T. Kottos, and A. Alù, Enhanced Sensing and Nondegraded Thermal Noise Performance Based on PT-Symmetric Electronic Circuits with a Sixth-Order Exceptional Point, Phys. Rev. Lett. **123**, 213901 (2019).

[44] N. A. Mortensen, P. A. D. Gonçalves, M. Khajavikhan, D. N. Christodoulides, C. Tserkezis, and C. Wolff, Fluctuations and noise-limited sensing near the exceptional point of parity-time-symmetric resonator systems, Optica **5**, 1342 (2018).

[45] W. Langbein, No exceptional precision of exceptional-point sensors, Phys. Rev. A **98**, 023805 (2018).

[46] M. Farhat, M. Yang, Z. Ye, and P.-Y. Chen, PT-Symmetric Absorber-Laser enables electromagnetic sensors with unprecedented sensitivity, ACS Photonics **7**, 2080 (2020).

[47] Keysight, *PathWave Advanced Design System (ADS)*, https://www.keysight.com/us/en/products/software/pathwave-design-software/pathwave-advanced-design-system.html.

[48] *OPA355 Data Sheet, Product Information and Support | TI.Com*, https://www.ti.com/product/OPA355.

[49] A. Paffi, M. Liberti, F. Apollonio, X. Ma, X. Du, and J. C. M. Hwang, in *2019 49th European Microwave Conference (EuMC)* (IEEE, Paris, France, 2019), pp. 89–92.